Open and closed conformations of a sub-80 kDa Chagas vaccine candidate defined by a cryo-EM led integrative approach

Sagar Batra [1], Timothy J Ragan [2], Asger Meldgaard Frank [3], Merve Kaplan [4], Claudia Lancey [2], Mahya Assadipapari [5,] Cuifeng Ying [5], Weston B. Struwe [5], Emma Hesketh [2], Lea Barfod [3,] and Ivan Campeotto[1]*

1. School of Biosciences, Division of Microbiology, Brewing and Biotechnology, University of Nottingham, Sutton Bonington Campus, LE12 5RD, UK
2. Leicester Institute of Structural and Chemical Biology, University of Leicester, Lancaster Road, Leicester, LE1 7RH, UK
3. Department of Immunology and Microbiology, Centre for Medical Parasitology, Faculty of Health and Medical Sciences, University of Copenhagen, Copenhagen, DK
4. Department of Biochemistry, University of Oxford, South Parks Road, Oxford OX13QU, UK
5. Advanced Optics & Photonics Laboratory, Department of Engineering, School of Science & Technology, Nottingham Trent University, Nottingham NG11 8NS, UK

*correspondence: ivan.campeotto@nottingham.ac.uk

Keywords: Chagas disease, cryo-EM, enzymology, SAX, MD, plasmonic optical tweezers

Abstract

Chagas disease, caused by the protozoan parasite *Trypanosoma cruzi*, remains a significant global public health concern. It affects an estimated eight million individuals worldwide, with the majority remaining undiagnosed. Despite its profound health impact in both endemic and non-endemic areas, no vaccine is available, and the existing therapies are outdated, producing severe side effects.

The 80kDa prolyl oligopeptidase of *Trypanosoma cruzi* (*Tc*POP) has been recently identified as a leading candidate for Chagas vaccine development. However, its three-dimensional structure has remained elusive for almost two decades since its discovery. We report the first three-dimensional structure of *Tc*POP in open and closed conformation, at a resolution of 3.0 and 2.5 Angstroms respectively, determined using single-particle cryo-electron microscopy. Multiple conformations were observed and were further characterized, using plasmonic optical tweezers.

To assess the immunogenic potential of *Tc*POP, we immunized mice and evaluated both polyclonal and monoclonal responses against the *Tc*POP antigen and its homologues. The results revealed unexpected cross-reactivity across prolyl POPs from other closely related parasites, but intriguingly, not towards the human homologue.

Altogether, our findings provide critical structural insights necessary to understand the immunogenicity of *Tc*POP for future Chagas vaccine development and diagnostic applications.

Additionally, our integrative approach indicated that stage-tilted acquisition can yield biologically relevant information for challenging sub-80kDa proteins and could adequately resolve the cryoEM structures. Consequently, this comprehensive strategy can significantly enhance the success rate in determining the structures of proteins that present challenges in characterization.

INTRODUCTION

Chagas disease is a chronic life-threatening parasitic disease caused by *Trypanosoma cruzi* and represents a significant health burden in 21 countries of Latin America (WHO 2023). Chagas continues to expand beyond endemic zones as a result of human migration and global warming [1], with 6 million infected people and 70 million individuals at risk of contracting the disease worldwide, leading to approximately 12,000 deaths per year (PANHO, [2]). The major transmission route is via the bite of insects belonging to the Triatomine species bug in endemic regions, although other routes include congenital transmission, organ transplants, blood transfusion or oral transmission [3].

Chagas disease becomes severe in a chronic infection wherein muscle cells in the heart and gut are compromised by both infection and immune responses against the parasite; this results in severe cardiac complications and heart failure in approximately 30% of patients with an estimated global economic hardship of $7.19 billion US per year [4]. Chagas is therefore, one of the major global neglected tropical diseases (NTDs). There is no vaccine and current therapy relies on the usage of the drugs nifurtimox and benznidazole [5], which and cause severe side effects including sterility, blindness, and deleterious effects in adrenal, colon, oesophageal and mammary tissue [6]. Additionally, therapies are effective only during the blood stage, which constitute the acute phase of the disease, whilst to date there is no drug against the intracellular chronic phase, which can continue decades after the acute infection, representing a “time bomb” on the health systems around the world.

To complicate the epidemiological scenario, due to the evolutionary plasticity of *Trypanosoma cruzi* genome, there are six discrete typing units (DTUs) [7] found to infect humans. An additional DTU has been identified in bats (*Tc*bat), for which transmission to humans has though not been yet reported [8]. DTUs differ in geographical distribution, ethnic distribution, clinical manifestations, and reservoir hosts, which include more than 150 species of mammals [9].

Diagnostic tools are often strain specific and unable to detect congenital transmission in newborn babies for the first 6 months, due to passive immunity from the mother, which can cause life-threatening complications later in life (PANHO and [10]). Amidst the challenges, a promising glimmer of hope has emerged. A member of the endopeptidase enzyme family, called *Trypanosoma cruzi* 80kDa prolyl-oligopeptidase (*Tc*POP, enzyme ID EC 3.4.21.26), has been identified as novel vaccine target for Chagas [11]. *Tc*POP is an enzyme expressed in both the extracellular blood trypomastigote and the replicative intracellular amastigote [12]. It degrades collagen and fibronectin extra-cellular matrix components on the host cells, allowing for parasite invasion. Its secretion into the blood during invasion, expression during all parasite stages and the more than 98–99% sequence conservations across DTUs [11] makes it an ideal candidate for vaccine development. This has been further supported in a murine model, as polyclonal antibodies against recombinant *Tc*POP, produced in *E. coli*, protected the mice from a lethal dose of the parasite [11].
No structure of parasite prolyl oligopeptidases (POPs) exists to date, despite POPs being reported in *Leishmania infantum (LiPOP,* [13]*)*, *Trypanosoma brucei (TbPOP)* [14]*)* and *Schistosoma mansoni (SmPOP)* [15] parasites.

The POP family is widely distributed across Eukaryotes and Prokayotes [16]. The closest protein homologues to *Tc*POP for which experimental structures are available are from *Haliotis discus hannai* (PDB code 6JCI), porcine muscle POP (PDB code 1QFM), *Pyrococcus furiosus* (PDB code 5T88) and Human POP (PDB 3DDU). Comparative homology modelling studies of *Tc*POP have been based on porcine POP [17] and predicted a cylindrical-shaped structure, consisting of a peptidase domain and a seven-bladed β-propeller domain with the substrate binding site and the canonical Asp, Ser, His catalytic triad, which located in the middle of the two domains [18].

*Tc*POP sequence is highly identical to LiPOP (63%), *Tb*POP (73%) and *Hu*POP (43%). We, therefore, also expressed these other POPs and immunised mice against *Tc*POP to nvestigate any evolutionary relationship or cross-reactivity related to epitope conservation across species.
Polyclonal and monoclonal antibodies (mAbs) were isolated and characterised from mice and the structure of TcPOP was solved by cryo-EM in closed and open conformation, aided by a plethora of in solution techniques, paving the way for new therapeutic interventions in Chagas disease.

MATERIALS AND METHODS

Bioinformatic analysis of *Tc*POP and *Tc*POP homologues

Protein sequences were extracted from the Uniprot database [19] for *Tc*POP (Q71MD6), *Tb*POP (Q38AG2), *Li*POP (A4ICB5) and *Hu*POP (P48147) and aligned in BLASTP [20] to retrieve the top 100 homologues of *Tc*POP and a phylogenetic tree was built in iTOL [21] after MSA generation in MUSCLE [22]. Comparative homology models were obtained with SWISS-MODEL [23] and when it became available for the scientific community, AlphaFold2 was used to obtain Ai-based models [24]. Phylogenetic analysis and sequence conservation mapping on *Tc*POP model was done using CONSURF [25]. Geometry of the models was assessed with MOLPROBITY [26] and 3D alignment performed in PyMOL [27].

Expression and purification of POPs by bacterial fermentation

The codon-optimised genes encoding for *Tc*POP and *Tc*POP orthologues were purchased from TWIST and inserted in the pET28(a)+ vector (Novagen). The resulting N-ter and C-ter His_6-tagged proteins were all recombinantly expressed and purified from *E. coli* NiCo21(DE3) strain (NEB). Cells were grown at 37°C supplemented with 2XYT medium (Melford) until OD_{600nm} at 0.6-0.8 was reached. Protein expression was induced using 0.5 mM isopropyl 1-thio-b-D-galactopyranoside (IPTG, Generon) using an 8L *in-situ* bioreactor (INFORS – Techfors S) at 100 rpm, for 18 hrs at 20°C leading with pH control at 7.0 (+/- 0.1) leading to 16 grams of bacterial cell pellet. Lysis was performed using BugBuster (Nalgene) and lysate was clarified by spinning at 50,000xg for 30 min at 4°C. Affinity chromatography was performed using Co^{+2}-NTA resin (Thermo Fisher). Washing buffer (50mM sodium phosphate, 500mM NaCl, 30mM Imidazole, pH 7.4) and elution buffer (50mM sodium phosphate, 500mM NaCl, 500mM Imidazole at pH 7.4) were used during affinity purification, followed by dialysis with 3.5 KDa MWCO Dialysis membranes (Pierce) at 4°C for 18hr against 20mM Hepes and 150mM NaCl at pH 7.4. Finally, the proteins were concentrated using 30kDa MWCO Amicon (Millipore) ultra-centrifugal filters to 10 mg/mL and immediately injected in gel filtration column S200 10/300 (Cytiva) equilibrated with 20mM Hepes and 150mM NaCl at pH 7.4. Elutions fraction containing protein were pooled together for further characterisation.

Western blot analysis

The sample were assessed on the SDS-PAGE gel (Bolt™ Bis-Tris Plus Mini Protein Gels, 4-12% gradient) (Page Ruler Pre-stained Ladder, ThermoFisher) and transferred to nitrocellulose membrane using Trans-Blot Turbo system (Biorad). Nitrocellulose membrane was incubated with His_6-tagged Monoclonal Antibody - HRP (Invitrogen) with 1:3000 v/v dilution in PBS-T, followed by the signal detection using SuperSignal West Pico PLUS Chemiluminescent Substrate (Cat. 34580, ThermoFisher) in an iBright system (Thermo Fisher).

Differential scanning fluorimetry

Stability measurement of prolyl oligopeptidases carried out using fluorescence assisted thermal unfolding assay. A fluorescence stain SYPRO Orange dye solution (ThermoFisher) was used and diluted to 5x concentration in 20 mM Hepes and 150 mM NaCl at pH 7.4. The assay was performed with a final protein concentration of 1 µM in a total volume of 20 µL. The temperature of the protein samples was gradually increased from 25°C to 95°C at a rate of 5°C per minute, using the Rotor-

Gene Q (Qiagen). Lastly, the data was analysed using non-linear regression method to determine the midpoint temperatures (T_m) of the thermal shift.

Enzymatic tests for POPs (main - AMC), for suppl. No effect of mAbs

Fluorogenic POP substrate Suc-Gly-Pro-Leu-Gly-Pro-7-amido-4-methylcoumarin (AMC) (HANGZHOU JHECHEM CO LTD) was diluted in PBS to 1-25 µM final concentrations in 96-well plates (ThermoFisher) to measure enzyme activity parameters in real time and as end-point reactions at 10 and 30 min, using Gen5™ Microplate Reader and Imager Software. Stock solutions were made in PBS and stored in aliquots at –20°C. The microplate readings were performed at excitation 360/40 nm and emission 460/40nm using BioTek Synergy LX Multimode plate reader.

Mice immunisations

The conducted animal research strictly conformed to the standards delineated by the Federation of European Laboratory Animal Science Associations (FELASA). Ethical clearance for the experimental methodologies was granted by the Danish Animal Experiment Inspectorate, as indicated by their approval number 2018-15-0201-01541. For the purpose of immunization, female BALB/c ByJR mice, aged six weeks, were obtained from Janvier Labs. Three mice were immunized intramuscularly with 20 µg of *TcPOP*, emulsified in 50% v/v AddaVax adjuvant (InvivoGen). This was followed by two additional intramuscular injections at biweekly intervals. A concluding intraperitoneal injection of 20 µg TcPOP in PBS was carried out two weeks post the last boost. Three days subsequent to the final injection, the mice were humanely euthanized for the extraction of spleen and blood.

Production, purification and conjugation of anti-*Tc*POP mAbs

After picking the best immune responders, hybridoma cell lines were generated by fusing splenocytes of immunized mice with myeloma cells following the instructions and materials from the ClonaCell-HY hybridoma cloning kit based on [28]. Hybridoma cell lines were harvested 14 days after the fusion and plated into 96-well culture plates in HT supplemented media. Screening of hybridoma cell lines producing antibodies specific to *Tc*POP was performed by ELISA, as described below. By single cell sorting using the FACSMelody (BD), monoclonal *Tc*POP-specific hybridoma cell lines were obtained. For large-scale mAb production, hybridoma cell lines were cultured in 4x250 mL cell culture flasks (Corning) as per manufacturer's instructions. Monoclonal antibodies were purified by affinity chromatography using a 5 mL protein G sepharose column (Cytiva) on an ÄKTAxpress system (Cytiva). Antibodies were eluted at 0.8 mg/mL in 0.1 M glycine buffer at pH 2.8 and immediately neutralized with 1/10 v/v 1M Trizma hydrochloride solution (Sigma Aldrich) at pH 9.0 to obtain the final pH at 7.4. Buffer exchange to 1 x PBS was performed using desalting column (Generon) and eluted protein was concentrated with 30kDa MWCO Amicon (Millipore) to 20 mg/mL. The 3 mAbs were specifically conjugated to HRP using EZ-*Li*nk™ Plus Activated Peroxidase Kit (ThermoFisher) and detected with ECL (Pierce) using iBright system.

Enzyme-*Li*nked Immunosorbent Assay (ELISA)

Antibody-producing hybridoma cells against *Tc*POP were ascertained through Enzyme-*Li*nked Immunosorbent Assay (ELISA). In summary, MaxiSorp flat-bottom 96-well ELISA plates (ThermoFisher) were coated with recombinant *Tc*POP (2 µg/mL in PBS) overnight at 4°C under shaking. Plates were there washed with PBS supplemented with 0.05% v/v Tween20 (PBS-T) and blocking performed for 1 hour with casein blocking solution (Pierce). The blocking solution was then removed, and replaced with 50 µL of hybridoma supernatant were added and incubated for 1 hour at RT under shaking. Plates were washed three times with PBS-T before undergoing incubation with 1:10000 v/v anti-mouse IgG (γ-chain specific) for 1hr, followed by three 5 min washes with PBS-T. The positive wells were identified by adding TMB plus2 (Kementec) for 20 mins and quenched using 0.2N sulfuric acid. Colorimetric and absorbance signals were measured at 450 nm. Data were analysed using GraphPAd (Prism).

Biophysical studies

Binding kinetics of *Tc*POP and anti-*Tc*POP mAbs using biolayer interferometry

Binding of anti-*Tc*POP mAbs to *Tc*POP were measured by kinetic experiments carried out on an Octet R4 (Sartorius). All samples were buffer exchanged into Sartorius Kinetics Buffer, according to the manufacturer's instructions. All measurements were performed at 200 µl/well in Sartorius kinetic buffer at 25°C in 96-well black plates (Greiner Bio-One, Cat# 655209). ProG (Cat. Nos. 18-5082, 18-5083, 18-5084) were used to immobilize anti-*Tc*POP mAbs for 1800s. Immunogens were four-fold serially diluted in kinetic buffer in the range of 64 nM to 4 nM. Assay was performed in three sequential steps with Octet BLI Discovery 12.2.2.20 software (Sartorius): Step 1, biosensor hydration and equilibration (300s); Step 2, immobilization of anti-*Tc*POP IgG1 mAbs on a ProG biosensor (600s); Step 3, wash and establish baseline (60s); Step 4, measure *Tc*POP association kinetics (1800s); and Step 5, measure *Tc*POP dissociation kinetics (600s). The acquired raw data for the binding of anti-*Tc*POP mAbs with *Tc*POP were processed and globally fit to a 1:1 binding model. Binding kinetics measurements were conducted in triplicate, and reported values represent the average. Data were analysed using Octet Analysis Studio 12.2.2.26 Software (Sartorius) and graphs produced using GraphPad (Prism).

Epitope binning studies using Bio-layer interferometry (BLI)

Anti-*Tc*POP mAb2 and anti-*Tc*POP mAb3 were applied sequentially to assess competition using BLI. Assay was performed in seven sequential steps with Octet® BLI Discovery 12.2.2.20 software (Sartorius): Step 1, biosensor hydration and equilibration (300s); Step 2, immobilization of *Tc*POP NiNTA biosensors (600s); Step 3, wash and establish baseline (60s); Step 4, measure anti-*Tc*POP mAb2 association kinetics (1800s); Step 5, measure anti-*Tc*POP mAb2 dissociation kinetics (600s); Step 6, measure anti-*Tc*POP mAb3 association kinetics (1800s); and Step 7, measure anti-*Tc*POP mAb3 dissociation kinetics (600s). The acquired raw data for the binding of anti-*Tc*POP mAbs with *Tc*POP were processed and globally fit to a 1:1 binding model with Octet Analysis Studio 12.2.2.26 Software (Sartorius). The binding kinetics measurements were carried out in three replicates. Values reported are the average among triplicates.

Estimation of apo-*Tc*POP using SEC-SAXS

SEC-SAXS was performed at the B21 beamline (Diamond *Li*ght Source, Oxon, UK). *Tc*POP was buffer exchanged into 20 mM HEPES and 150 mM NaCl (pH 7.4) at 277K before data collection. Using an Agilent 1200 HPLC system, 50 µL of *Tc*POP at 8 mg/mL was loaded onto a Shodex KW-403 column. X-ray intensity data were collected as the eluent moved from the column to the beam at a flow rate of 0.16 mL/min. The intensity was plotted against its angular dependants q ($q = 4\pi\sin\theta/\lambda$) while, system operated with an exposure time of 3s at 12.4 keV (1Å) using a EIGER 4 M detector. Data were analyzed using the ATSAS program suites and plotted using GNOM.

Mass photometry

Buffer optimisation for TcPOP

Conducted mass photometry experiments using the Refeyn OneMP mass photometer, cleaning coverslips and gaskets with 100% isopropanol and water. Measurements, performed in triplicate, involved systematic optimizations of pH values in the range 7.0-8.0 and ionic strength with NaCl concentration range 50-300mM within a 20 mM BTP buffer. Protein was diluted in buffer to a final concentration of 120 nM into a gasket well, followed by focal point acquisition and data analysis using Refeyn AcquireMP 2.3.1 software. Mass photometry movies (6000 frames, 20 frames per sec) were captured within a 10.8 × 10.8 µm field and processed with Refeyn DiscoverMP 2.3.0 software. Robust data analysis ensued, leveraging a contrast-to-mass (C2M) calibration approach. Calibration involved introducing 3 µL of a 1:100 v/v pre-diluted NativeMark standard (LC0725, Thermo Scientific) to an acquisition well, yielding masses (66, 146, 480, 1048 kDa) that informed the calibration curve employed in DiscoverMP software. Experiments were performed at the Leicester Institute for Structural and Chemical Biology (LISCB, University of Leicester, UK).

mAb2 and mAb3 binding to TcPOP measuraments

Mass photometry (MP) measurements were conducted using a Refeyn TwoMP (Refeyn Ltd) as previously described [29]. Briefly, glass coverslips (High Precision No. 1.5H, Marienfeld Superior) were cleaned by sequential sonication with Milli-Q H_2O, 50% isopropanol and again Milli-Q H_2O. Cleaned coverslips were dried using nitrogen flow. CultureWell™ reusable gaskets (3 mm diameter x 1 mm depth, Grace Bio-Labs) were used to assemble sample chambers. Coverslips were placed on the MP sample stage and a single gasket was filled with 20 µL DPBS (wo/ calcium and magnesium, pH 7.4, ThermoFisher Scientific) to find focus. *Tc*POP, mAb2 and mAb3 were measured separately at a final concentration of 20 nM. For *Tc*POP-antibody binding assays, 5 µM *Tc*POP was mixed with 5 µM mAb2 or mAb3 in a 1.5 mL Eppendorf tube at a 1:1 ratio (v/v). The sample mixture was equilibrated for 10 minutes and diluted 1:100 before data acquisition. Acquisition settings were adjusted within AcquireMP (2023 R1.1, Refeyn Ltd) as a large field of view, frame binning = 2, frame rate = 128.2 Hz, pixel binning = 6, exposure time = 7.65 ms. Movies were taken over 60 seconds. Mass calibration was performed using an in-house protein standard including 90-720 kDa oligomers. Data was analysed and histograms were created with Discover MP (v2023 R1.2, Refeyn Ltd). Experiments were performed at the New Biochemistry building (University of Oxford, UK).

MD simulations

Atomics coordinates of *Tc*POP were retrieved from AlphaFold database. To calculate the conformational dynamics of *Tc*POP, all-atom molecular dynamics simulations were conducted on Augusta supercomputer cluster at the University of Nottingham using GROMACS 2021.2-fosscuda-2020b package. GROMOS 54a7 forefield was applied and hydrogen atoms were incorporated using the pdb2gmx module, and topology files were generated under periodic boundary condition (PBC) employing a cubic periodic cell. The protein was centrally placed, solvated using simple point charge (SPC) 216 water molecule and positioned 1 nm from the edges, with NaCl counter ions added for system neutralization.

Following energy minimization, the canonical ensemble (NVT) underwent equilibration for 100 ps without pressure coupling and Berendsen thermostat was initially applied. Subsequently, temperature (298 K) was maintained by velocity rescaling with a stochastic term, while the isothermal-isobaric ensemble (NPT) with a 1 bar pressure for 100 ps, using the Parrinello–Rahman method, was implemented. The LINCS algorithm constrained H-bonds, and the MD simulations ran for 500 ns with a 2 fs time step. The resulting trajectory was analysed using inbuilt utilities of the GROMACS[30].

Cryo-EM sample preparation, data collection and processing

Cryo-EM grid preparation

Homogeneous samples from SEC purified in 20mM HEPES, 150mM NaCl at pH 7.4 were freshly used to prepare the grids. Fraction corresponding to the SEC peak at 15 mls (Fig.S2) was used at a final concentration of 0.2mg/mL. Firstly, cryoEM grids, R1.2/1.3 carbon, Au 300 (Quantifoil), were glow discharged in the presence of amylamine for 30 seconds at 10 mA on a Quorum GloQube glow-discharge unit. Four microliters of the freshly prepared *Tc*POP sample were applied to the grid and blotted for 3 sec, with blot force 10, prior to flash-cooling in liquid ethane using a Vitrobot Mark IV (FEI ThermoFisher), set at 4 °C and 100% humidity.

CryoEM data collection

CryoEM grids were imaged using 300KeV Titan Krios G3 (ThermoFisher Scientific) transmission electron microscope (Midlands Regional Cryo-EM Facility at the University of Leicester) at a calibrated pixel size of 0.656 Å. Electron micrographs were recorded using a K3/GIF (Gatan Imaging Filter) direct electron detector (Gatan Inc.) and EPU automated data acquisition software (ThermoFisher Scientific). Micrograph movies were recorded with 75 fractions, in super resolution, binned by 2 and a total dose of 77 e^-/pix (dose rate of 15 e-/pix/s), To improve the distribution of particles views data were collected at 0°, 30° and 35°. At 0° tilt (Dataset 1) the defocus range was collected between -2.3 and -0.8 µm, in regular intervals. At 30° and 35° tilt (dataset 2), the defocus was set to -1.2 µm.

Cryo-EM image processing

All image processing was carried out on the CryoEM computational cluster, University of Leicester. Micrographs were pre-processed using Relion5-beta, [31] sample motion during acquisition was corrected using RELIONs own implementation with dose-weighting activated, followed by CTF estimation using CTFFIND4.1 [32]. Particles were picked on aligned micrographs using Topaz [33] via template matching on the untilted dataset, then extracted with a box size – 256pixels (corresponding to 168Å) binned by 4 to 2.624 Å/pix. Initially each dataset (i.e. untilted and tilted) was processed separately. For each dataset, a subset of micrograph was processed initially. Particles were classified in 2D and classes which showed high resolution features were selected and used to produce *ab-initio* model generation in RELION 5-beta. Analysis of the 3D initial models revealed "open" and "closed" conformations. The full dataset was classified in 3D (with blush regularisation) and the classes were inspected and subcategorised into open and closed particles. Refined centre locations were used to re-extract the particles at 1.312 Å/pix. Further rounds of 3D classification (with Blush regularisation) were performed to separate two population of homogeneous particles subsets (open and closed). The tilted and untilted datasets were then merged. Further rounds of 3D classification were then carried out with Blush regularisation. "Open" and "Closed" maps were refined using AutoRefine (with Blush regularisation) prior to 2D classification without alignment to remove remaining 'junk' particles. The final particle set was then unbinned via Bayesian polishing followed by CTF Refinement (using sequential beam tilt; magnification anisotropy; defocus/astigmatism steps). A round of 3D AutoRefine with Blush regularisation yielded the final maps (Table 1).

Data collection and processing	Dataset 1 (untilted)	Dataset 2 (tilted)
Magnification (nominal)	130,000 x	130,000 x
Voltage (kV)	300	300
Stage (Z) tilt	0	-30 and -35
Aberration free image shift (AFIS)	Yes (12 µm)	No
Electron exposure (e^{-}/Å^2)	76.43	77.59
Illuminated area (µm)	0.65	0.57
Fractionation	75	75
Defocus range (µm)	-2.3 to -0.8	-1.2µm
Pixel size (Å)	0.656	0.656
Total micrographs (no.)	20,080	2,292
Total particle images (no.)	45,400,101	2,525,462
Closed conformation final particle images (no.)	847,556	395,555
Open conformation final particle images (no.)	518,841	420,986
Map resolution (Å)	Open: 3.00Å Closed: 2.54Å	
FSC threshold	0.143	0.143
Map resolution range (Å)	2.93Å - 4.20Å	2.49Å – 3.53Å
Initial model used (PDB code)	*Ab initio*	*Ab initio*

Table 1 Cryo-EM data collection, refinement and validation statistics

Cryo-EM model fitting and refinement.

Open and Closed conformation of *Tc*POP was docked in the CryoEM map using phenix.*dock_in_map*. Both maps were refined and validated using *phenix.real_space_refine.* Lastly, chimeraX was used to generate visual molecular graphics.

Data availability

CryoEM reconstructions will be deposited to the EM Data Bank (EMDB). Coordinates will be deposited to the Protein Data Bank (PDB). Accession codes will be updated upon publication.

Plasmonic Optical nanotweezers: samples preparation and data collection

We used a plasmonic optical tweezers setup which is a modified modular optical tweezers system (OTKB/M, Thorlabs) in Advanced Optics and Photonics Lab at the Nottingham Trent University with a 852 nm Fabry-Perot laser diode (FPL852S, Thorlabs) [34]. The laser beam was polarised perpendicular to the centre-to-centre line of two circles of the double nanohole (DNH) structure by using a polariser and a half-wave plate and was collimated and focused on the DNH by a 60X air objective (NA 0.85, Nikon). All trappings were performed at a laser power of 25 mW [35] The transmitted laser intensity was then converted to a voltage signal via a silicon avalanche photodiode (APD120A, Thorlabs) and recorded by a data acquisition card with a sampling rate of 1 MHz. The recorded voltage data (transmission traces) were normalised and filtered using in-house MATLAB scripts, which included a zero-phase Gaussian low-pass filter (MATLAB *filtfilt.m*) with cut-off frequencies of 10kHz, 1kHz, 100Hz, and 10Hz. Probability density function (PDF) were calculated by using MATLAB function *ksdensity.m*. More information on this specific set-up have been previously reported [36]. SEC Purified *Tc*POP was used at 1 µM concentration in PBS. DNHs were sealed into the flow cell using cover glass with a double-sided tape as a spacer, providing a microfluidic channel with 3.5 µL volume. The solution was delivered to the flow cell using a 12-way valve and a syringe pump. Initially, *Tc*POP was infused in the chamber to achieve trapping followed by the sequential infusions of 1µM, 10µM and 100 µM substrate Suc-Gly-Pro-Leu-Gly-Pro-AMC to the flow cell at a flow rate of 2 µL/min.

Results

Expression and purification of *Tc*POP and *Tc*POP homologues

*Tc*POP was expressed in *E. coli* using bacterial fermentation (Materials and Methods), which allowed to overcome the hurdle of extremely low expression in batch (~ 0.05 mg/L) (Fig. 1A), whilst the other homologue *Tb*POP, *Li*POP and *Hu*POP were expressed in batch with higher protein yields (0.8-2.0 mg/mL). All POPs are active and show comparable end-point kinetics using the substrate-mimicking Suc-Gly-Pro-Leu-Gly-Pro-AMC fluorogenic peptide (Material and Methods) as previously reported for this family of enzymes [37] (Fig. S1).

All POPs were purified by SEC (Fig. S2) analysed SEC-MALS (*Tc*POP: 73.4 (±2.1%) kDa,*Tb*POP: 73.7 (±1.6%) kDa ,*Li*POP: 75.7 (±3.5%) kDa, *Hu*POP: 85.3 (±1.71%) kDa) (Fig.1A-D) and their thermostability measure by DSF (Fig. S3). All proteins are monomeric and monodisperse in solution.

An AlphaFold model of *Tc*POP, predicted its composition to consist of an α/β -hydrolase domain containing the catalytic triad Ser548-Asp631-His667 and a seven-bladed beta-propeller non-catalytic domain. That correlates with the previously determined structure of porcine POP (PDB code 1QFM) [18].

Phylogenetic analysis and sequence conservation mapping on *Tc*POP model evaluated conserved and variable regions locate in both catalytic and non-catalytic domains (Fig.2A), nonetheless, previous docking experiments located the substrate binding site in the middle of the two domains [18] that phylogenetically corresponds to the region of high variability (Fig.2A).

Anti-*Tc*POP responses reveal distinct specificity and cross-reactivity

To characterize the cross-reactive potential of antibodies directed against *Tc*POP mice were immunized with recombinant *Tc*POP. Homologous proteins with high amino acid identity from *Leishmania infantum* (*Li*POP, 63%), *Trypanosoma brucei* (*Tb*POP, 73%), and *Homo sapiens* (*Hu*POP, 43%) were expressed and purified to investigate any potential cross-reactivity highlighting evolutionary conservation of epitopes as expected from the phylogenetic analysis in iTOL (Fig.S4).

Three anti-*Tc*POP mAbs were isolated and screened by ELISA to test specificity against all POPs (Fig.2 and Fig3). For *Tc*POP antibody titres were positive at 1 µg/ml for mAb1 and 0.1 µg/ml for mAbs 2 and 3 (Fig.3A), whereas *Li*POP, *Tb*POP and *Hu*POP did not showed any binding towards any anti-*Tc*POP mAbs. Additionally, *Tc*POP-specific serum ELISA were performed against all four POPs to identify any cross-reactivity. Polyclonal anti-*Tc*POP IgG was detected in anti-*Tc*POP mice blood serum against *Tc*POP, *Tb*POP, and *Li*POP, with a weaker signal for *Hu*POP at serially diluted serum concentrations. HRP-conjugation of anti-*Tc*POP mAbs revealed the presence of both linear and conformational epitopes, as confirmed by Western blotting (Fig. 4A). Here, ELISA data suggested potential epitope conservation across parasite species but not towards *Hu*POP (Fig. 2B-E).

The BLI-based binding profile for immobilised anti-*Tc*POP mAbs against *Tc*POP showed higher binding affinity to *Tc*POP for anti-*Tc*POP mAb2 (K_D <1pM, K_a (1/Ms) 2.3 x 10^5, K_{diss} (1/s) < 10^{-7}) and anti-*Tc*POP mAb3 (K_D <1pM, K_a (1/Ms) 3.1 x 10^5, K_{diss} (1/s) < 10^{-7}). Instead, anti-*Tc*POP mAb1 exhibited comparatively weak binding (K_D < 3.2 nM, K_a (1/Ms) 7.1 x 10^4, K_{diss} (1/s) 6.2 x 10^{-4}) (Fig. 4B-D) as well as association and dissociation parameters. In fact, the best two mAbs, mAb2 and mAb3, were used to perform a sequential affinity binding with association and dissociation length of 1800s and 600s respectively. Both mAbs showed detectable association and dissociation (K_D <1pM, K_a (1/Ms) >10^7, K_{diss} (1/s) < 10^{-7}) indicating competition for different epitopes (Fig. 4E).

Mass photometry measurements of individual *Tc*POP, mAb2 and mAb3 was 85, 151 and 151 kDa respectively with only a single peak present in each MP spectrum (Fig.S5). Interaction studies revealed similar binding between *Tc*POP and both antibodies. A peak corresponding to 1:1 (mAb to *Tc*POP) was observed at 233 kDa with a relative abundance of 17% (*Tc*POP-mAb2) and 19% (*Tc*POP-mAb3). No evidence of higher-order binding was found (Fig. 5).

*Tc*POP characterisation in solution

SEC-SAXS, mass photometry

SEC-SAXS data on purified *Tc*POP are in agreement with the AlphaFold model with an estimated molecular weight of 78.5 kDa (Bayesian inference) [38] indicating a globular conformation with no aggregation (Fig. 6A), as confirmed by, Kratky (Fig. 6B-C), Guinier analysis and Porod plots (Fig. S6). Mass photometry also allowed to identify the best buffer conditions in term of ionic strength and pH values (Fig. D-E). This information was exploited for cryo-EM grid preparation to increase sample homogeneity and also to analyse TcPOP and interaction with mAb2 and mAb3 (Fig.S5).

MD simulation of *Tc*POP

To understand the intrinsic dynamics of *Tc*POP, molecular dynamics simulations were performed using the AlphaFold model from Uniprot (Q71MD6) as the starting point for 500ns simulations, which showed notable transitions in Root Mean Square Deviation (RMSD) around 290ns (Fig.7A), while Radius of Gyration (Rg) (Fig.S6-A) and Solvent Accessible Surface Area (SASA) (Fig. S6B)

underwent complementary contraction for the first 300ns, followed by significant expansion up to 500ns, indicating substantial conformational changes. Root Mean Square Fluctuations (RMSF) identified residues L192 – K198 and T306 – S333 as highly unstable (Fig. 7C), and particularly in the non-catalytic β-propeller domain compared to the catalytic α/β hydrolase domain (Fig.7A). The Gibbs free energy landscape analysis identified four significant minima basins, providing insights into local and global minima in a 2D and 3D projection of FEL, as described previously [39] (Fig.7D-E).

Determination of Cryo-EM structure of *Tc*POP in multiple conformations

*Tc*POP structure determination using single particle CryoEM

We analysed the structure of TcPOP using single particle analysis (SPA) cryo-EM. The initial data collection comprised of 20,080 micrographs revealed severe preferential orientation and a reliable map was not produced (Fig.S8). We experimented with cryoEM grid preparation by addition of detergent, support films and glow discharge parameters but were unable to improve the orientation distribution. We therefore tilted the grids to 30° and 35° to increase the number of views visualised in the electron micrographs. This significantly improved the number of views and the map produced was drastically improved with continuous density and minimal anisotropic features (Fig.S8). 3D classification revealed two distinct conformations of *Tc*POP i.e. open and closed (Fig.8), indicating conformational heterogeneity in the dataset. Closed and open conformation models obtained from AlphaFold and homology modelling (using PDB 3IUJ), respectively, were then docked into their respective CryoEM maps and then refined (Table 2).

Refinement parameters	Closed conformation	Open conformation
Map resolution (masked)	3.54Å	4.02Å
Map resolution (unmasked)	3.55Å	4.03Å
FSC (model) (masked) = 0.143	2.28Å	3.35Å
Corelation Coefficient (masked)	0.75	0.55
Ramachandran favoured	95.09%	93.12

Table 2 Cryo-EM statistics for closed and open conformation from real-space refinement in PHENIX [40].

Plasmonic Optical nanotweezers*:*

Aperture-based plasmonic nanotweezers revealed the conformational dynamics of single, unmodified *Tc*POP (Fig.S9) *Tc*POP trapping events were detected by changes in transmission levels, filtered at a cutoff frequency of 1 kHz, whilst time traces of $\Delta T/T_0$ of *Tc*POP trapped in the absence of substrate AMC (blue and purple, Fig. S9), and with 100 μM AMC substrate introduced to the trapping site. Addition of substrate at 100 μM concentration led to larger fluctuations in transmission, indicating *Tc*POP exhibiting greater dynamic fluctuations during enzymatic cycles than in its apo- state. However, in the absence of a substrate, distinct signal fluctuations were observed above the background of Brownian motions in the trapping well, suggesting free transition of multiple conformations of *Tc*POP in solution. This is further corroborated by distinct peaks in the probability density functions (PDFs) (Materials and Methods).

Discussion

Structural data on Chagas antigens are desperately needed to guide vaccine development and design of diagnostic solutions. Such data are invaluable to initiate structure-based immunogen design strategies which focus the immune response towards key conserved epitopes [41] and to identify regions within the target protein suitable for drug design.

*Tc*POP is one of the leading validated candidates for a Chagas vaccine, given its high sequence conservation across the six genotypes (or DTUs) of *Trypanosoma cruzi* strains.

The three-dimensional structure of *Tc*POP remained elusive for almost two decades since a model was proposed in 2005 [18]. Several attempt to crystalise parasite POPs in our lab, including *Tc*POP, did not succeed, despite the usage of starting protein concentrations up to 500 microM for crystallisation screening (equivalent to ~ 40 mg/mL). Closed conformations for *Tc*POP homologues have been previously reported using protein crystallography from porcine POP (PDB code 1QFM), *Hu*POP with an irreversible inhibitors (PDB 3DDU), to lock the enzyme in the closed state. However, in our knowledge, neither fully open nor fully close conformations have been solved before ours without the aid of additives. High solubility was a characteristic of not only of *Tc*POP but also of other POPs reported in this manuscript, and this is likely to be linked to their function of being secreted in the blood to perform degradation of the extracellular host matrix. In fact, *Tc*POP possess 33 Lys residues, out of which 13 Lys are located on solvent accessible surface, therefore likely to prevent crystal contacs required to promote crystallisation. Methods have been developed to reduce protein entropy by lysine methylation [42] but we opted not to use this strategy, as this could have compromised antigenicity by altering potential keys residues involved in epitope-paratope interaction.

Immunizing mice with recombinant *Tc*POP led to the production of polyclonal antibodies that showed cross-reactivity with *Leishmania infantum* and *Trypanosoma brucei* homologs, indicating conserved epitopes among these parasites. However, the weaker response to human homolog suggests a possible divergence in epitope conservation. This approach not only underscores the potential for developing cross-protective vaccines against related parasite species but also emphasizes the precision in targeting pathogen-specific epitopes while minimizing cross-reactivity with human proteins for diagnostic applications. The identification of both linear and conformational epitopes further enriches the understanding of antigen-antibody interactions.

AlphaFold model of closed conformation of *Tc*POP explained the dynamic nature of *Tc*POP showed significant transition in the Cα-backbone during the course of the MD simulation. Also, the simulation suggested such transition occur between the two domains of *Tc*POP exposing their catalytic site during enzyme activity, importantly, β-propeller domain contributed to a high degree of movement and unstablity, whereas, α/β hydrolase domain remained comparatively stable (Movie 1). Moreover, the Gibbs free energy landscape of *Tc*POP indicated scattered blue spots, representing four major local or global energy minima, therefore, provided valuable insights into the presence of different metastable states (Fig. 7D-E)

We, therefore, decided to analyse the structure using cryo-EM, despite the challenge to date of resolving sub-80 kDa molecules, due to low image contrast [43]. To ensure the quality of samples before cryo-EM, we implemented a quality control pipeline, which included SEC-SAXS in solution studies followed by assessment of the best buffer conditions using MP to screen for the best conditions for monodispersion.

Our approach led to structure determination of *Tc*POP structure at 2.5 and 3.0 , respectively in closed and open conformation, resolution in multiple conformations, which is one of the smallest cases and at the highest resolution reported in term of resolving multiple enzyme conformations in vitreous state by single-particle cryo-EM [44]. Two conformations of *Tc*POP could be easily identified in 3D

classification spanning from fully closed to fully open with an overall motion of ~ 22° between the domains, with the z-axis of rotation centred on Gly 424. The evident stability of the α/β hydrolase domain observed in both open and closed conformations ad well as in those from aligned CryoEM maps, suggest possible region which are expose to the immune system when the enzyme is secreted in the blood, therefore likely to include potential epitopes.

To confirm that these experimentally observed conformations exist in solution, optical tweezers studies were performed in presence and absence of substrate-mimicking peptide. Recent advances in plasmonic nanotweezers allowed to sample conformational fluctuations in single proteins in solution [45]. Our data show that *Tc*POP clearly fluctuates between open and closed conformations independently from the presence of the substrate, confirming that the observed open and closed states occur in solution and are observed without the usage of additive. However, the presence of the substrate-mimicking peptide affects the frequency at which the enzyme opens and closes.

The intrinsic conformational heterogeneity in solution can pose great challenges to the structure determination by Cryo-EM, as multiple conformations merge into a single conformation often lead to preferential orientation and eventually producing lower-resolution 3D reconstruction, which requires the collection of large number of micrographs especially for small molecules, often in the order of thousands. Here, we have successfully characterized the open-close transition of *Tc*POP through a synergistic combination of *in silico*, structural, and in solution techniques. We propose expanding this methodology for regular investigations of small proteins of sub-80kDa size, especially when recalcitrant to crystallography approaches and alternating conformations in solution, with the addition of tilted data collection, which allowed us to reduce preferential orientation and reveal more structural details.

We envisage the possibility to extend this approach to other targets, allowing to predict the number of 3D classes in vitreous state using cryo-EM data based on MD simulations, understanding conformational heterogeneity at the early stages of CryoEM data processing and therefore, potentially aiding future software developments towards this goal.

We provide experimental evidence on the transition between open and closed conformation, which will be invaluable to determine which regions of TcPOP should be targeted to block the enzyme in either conformation, therefore to aid the development of novel and much needed anti-parasitic therapeutic agents.

Additionally, we characterised three anti-*Tc*POP monoclonal antibodies, which will be exploited for diagnostic and therapeutic applications, as *Tc*POP is shredded in the blood.

Our study, in the longer-term, will allow us to initiate a structure-guided development of a Chagas vaccine prototype, which is desperately needed in the fight against this major neglected disease.

Acknowledgements

We would like to acknowledge: Dr Nathan Cowieson for assisting data collection at B21 beamline (Diamond Light Source), Dr David Staunton (University of Oxford) for data collection of SEC-MALS, Dr Lei Xu (NTU) and Prof. Rahmani Mohsen (NTU) for advise on data analysis of plasmonic optical tweezers experiments. Additionally, we would like to thank, Anu Itansanmi-Ogundayomi (Federal University of Technology Akure, Nigeria), Dr Jody Winter (NTU) and Dr Richard Cowan (University of Leicester).

The project was funded by: Wellcome grant 204801/Z/16/Z (IC), Royal Society grant IES\R2\232167 (IC. SB is supported by the Nottingham Trent Doctoral School studentship and LB is funded by Novo Nordisk Foundation (NNF170C0026778). We acknowledge The Midlands Regional CryoEM Facility

552 at the Leicester Institute of Structural and Chemical Biology (LISCB), major funding from MRC
553 (MC_PC_17136).

554 1. Medone P, Ceccarelli S, Parham PE, Figuera A, Rabinovich JE. The impact of climate change
555 on the geographical distribution of two vectors of Chagas disease: implications for the force of
556 infection. Philos Trans R Soc Lond B Biol Sci. 2015;370(1665). Epub 2015/02/18. doi:
557 10.1098/rstb.2013.0560. PubMed PMID: 25688019; PubMed Central PMCID: PMCPMC4342964.
558 2. Lee BY, Bacon KM, Bottazzi ME, Hotez PJ. Global economic burden of Chagas disease: a
559 computational simulation model. Lancet Infect Dis. 2013;13(4):342-8. doi: 10.1016/s1473-
560 3099(13)70002-1 PMID - 23395248.
561 3. Coura JR. The main sceneries of Chagas disease transmission. The vectors, blood and oral
562 transmissions--a comprehensive review. Mem Inst Oswaldo Cruz. 2015;110(3):277-82. Epub
563 20141202. doi: 10.1590/0074-0276140362. PubMed PMID: 25466622; PubMed Central PMCID:
564 PMCPMC4489464.
565 4. Bonney KM, Luthringer DJ, Kim SA, Garg NJ, Engman DM. Pathology and Pathogenesis of
566 Chagas Heart Disease. Annu Rev Pathol. 2019;14:421-47. Epub 2018/10/26. doi: 10.1146/annurev-
567 pathol-020117-043711. PubMed PMID: 30355152; PubMed Central PMCID: PMCPMC7373119.
568 5. Mazzeti AL, Capelari-Oliveira P, Bahia MT, Mosqueira VCF. Review on Experimental
569 Treatment Strategies Against Trypanosoma cruzi. J Exp Pharmacol. 2021;13:409-32. Epub 20210331.
570 doi: 10.2147/JEP.S267378. PubMed PMID: 33833592; PubMed Central PMCID: PMCPMC8020333.
571 6. Castro JA, de Mecca MM, Bartel LC. Toxic side effects of drugs used to treat Chagas' disease
572 (American trypanosomiasis). Hum Exp Toxicol. 2006;25(8):471-9. doi:
573 10.1191/0960327106het653oa. PubMed PMID: 16937919.
574 7. Joselin DV, Ignacio M, Angel RM, Gabriel GG, Rodrigo Isaias LV, Victor SC, et al. Multiple
575 Discrete Typing Units of Trypanosoma cruzi Infect Sylvatic Triatoma dimidiata and Panstrongylus
576 rufotuberculatus in Southeast Mexico. Am J Trop Med Hyg. 2021;105(4):1042-9. Epub 2021/08/17.
577 doi: 10.4269/ajtmh.20-1574. PubMed PMID: 34398820; PubMed Central PMCID: PMCPMC8592174.
578 8. Lima L, Espinosa-Alvarez O, Ortiz PA, Trejo-Varon JA, Carranza JC, Pinto CM, et al. Genetic
579 diversity of Trypanosoma cruzi in bats, and multilocus phylogenetic and phylogeographical analyses
580 supporting Tcbat as an independent DTU (discrete typing unit). Acta Trop. 2015;151:166-77. Epub
581 20150719. doi: 10.1016/j.actatropica.2015.07.015. PubMed PMID: 26200788.
582 9. Breniere SF, Waleckx E, Barnabe C. Over Six Thousand Trypanosoma cruzi Strains Classified
583 into Discrete Typing Units (DTUs): Attempt at an Inventory. PLoS Negl Trop Dis.
584 2016;10(8):e0004792. Epub 2016/08/30. doi: 10.1371/journal.pntd.0004792. PubMed PMID:
585 27571035; PubMed Central PMCID: PMCPMC5003387.
586 10. Porras AI, Yadon ZE, Altcheh J, Britto C, Chaves GC, Flevaud L, et al. Target Product Profile
587 (TPP) for Chagas Disease Point-of-Care Diagnosis and Assessment of Response to Treatment. PLoS
588 Negl Trop Dis. 2015;9(6):e0003697. Epub 20150604. doi: 10.1371/journal.pntd.0003697. PubMed
589 PMID: 26042730; PubMed Central PMCID: PMCPMC4456144.
590 11. Bivona AE, Alberti AS, Matos MN, Cerny N, Cardoso AC, Morales C, et al. Trypanosoma cruzi
591 80 kDa prolyl oligopeptidase (Tc80) as a novel immunogen for Chagas disease vaccine. Plos Neglect
592 Trop D. 2018;12(3):e0006384 - 23. doi: 10.1371/journal.pntd.0006384.
593 12. Grellier P, Vendeville S, Joyeau R, Bastos IM, Drobecq H, Frappier F, et al. Trypanosoma cruzi
594 prolyl oligopeptidase Tc80 is involved in nonphagocytic mammalian cell invasion by
595 trypomastigotes. Journal of Biological Chemistry. 2001;276(50):47078 - 86. doi:
596 10.1074/jbc.m106017200.

13. Lasse C, Azevedo CS, Araújo CNd, Motta FN, Andrade MA, Rocha AP, et al. Prolyl Oligopeptidase From Leishmania infantum: Biochemical Characterization and Involvement in Macrophage Infection. Front Microbiol. 2020;11:1060. doi: 10.3389/fmicb.2020.01060 PMID - 32547514.
14. Bastos IM, Motta FN, Charneau S, Santana JM, Dubost L, Augustyns K, et al. Prolyl oligopeptidase of Trypanosoma brucei hydrolyzes native collagen, peptide hormones and is active in the plasma of infected mice. Microbes Infect. 2010;12(6):457-66. Epub 20100224. doi: 10.1016/j.micinf.2010.02.007. PubMed PMID: 20188209.
15. Fajtova P, Stefanic S, Hradilek M, Dvorak J, Vondrasek J, Jilkova A, et al. Prolyl Oligopeptidase from the Blood Fluke Schistosoma mansoni: From Functional Analysis to Anti-schistosomal Inhibitors. PLoS Negl Trop Dis. 2015;9(6):e0003827. Epub 20150603. doi: 10.1371/journal.pntd.0003827. PubMed PMID: 26039195; PubMed Central PMCID: PMCPMC4454677.
16. Kaushik S, Sowdhamini R. Distribution, classification, domain architectures and evolution of prolyl oligopeptidases in prokaryotic lineages. BMC Genomics. 2014;15(1):985. Epub 20141118. doi: 10.1186/1471-2164-15-985. PubMed PMID: 25407321; PubMed Central PMCID: PMCPMC4522959.
17. Fulop V, Bocskei Z, Polgar L. Prolyl oligopeptidase: an unusual beta-propeller domain regulates proteolysis. Cell. 1998;94(2):161-70. doi: 10.1016/s0092-8674(00)81416-6. PubMed PMID: 9695945.
18. Bastos Izabela MD, Grellier P, Martins Natalia F, Cadavid-Restrepo G, de Souza-Ault Marian R, Augustyns K, et al. Molecular, functional and structural properties of the prolyl oligopeptidase of Trypanosoma cruzi (POP Tc80), which is required for parasite entry into mammalian cells. Biochem J. 2005;388(1):29-38. doi: 10.1042/bj20041049 PMID - 15581422.
19. UniProt C. UniProt: the Universal Protein Knowledgebase in 2023. Nucleic Acids Res. 2023;51(D1):D523-D31. Epub 2022/11/22. doi: 10.1093/nar/gkac1052. PubMed PMID: 36408920; PubMed Central PMCID: PMCPMC9825514.
20. Sayers EW, Beck J, Bolton EE, Brister JR, Chan J, Comeau DC, et al. Database resources of the National Center for Biotechnology Information. Nucleic Acids Res. 2024;52(D1):D33-D43. Epub 2023/11/23. doi: 10.1093/nar/gkad1044. PubMed PMID: 37994677; PubMed Central PMCID: PMCPMC10767890.
21. Letunic I, Bork P. Interactive Tree Of Life (iTOL) v5: an online tool for phylogenetic tree display and annotation. Nucleic Acids Res. 2021;49(W1):W293-W6. Epub 2021/04/23. doi: 10.1093/nar/gkab301. PubMed PMID: 33885785; PubMed Central PMCID: PMCPMC8265157.
22. Edgar RC. MUSCLE: a multiple sequence alignment method with reduced time and space complexity. BMC Bioinformatics. 2004;5:113. Epub 2004/08/21. doi: 10.1186/1471-2105-5-113. PubMed PMID: 15318951; PubMed Central PMCID: PMCPMC517706.
23. .
24. Baek M, DiMaio F, Anishchenko I, Dauparas J, Ovchinnikov S, Lee GR, et al. Accurate prediction of protein structures and interactions using a three-track neural network. Science. 2021;373(6557):871-6. Epub 2021/07/21. doi: 10.1126/science.abj8754. PubMed PMID: 34282049; PubMed Central PMCID: PMCPMC7612213.
25. Ashkenazy H, Abadi S, Martz E, Chay O, Mayrose I, Pupko T, et al. ConSurf 2016: an improved methodology to estimate and visualize evolutionary conservation in macromolecules. Nucleic Acids Res. 2016;44(W1):W344-50. Epub 2016/05/12. doi: 10.1093/nar/gkw408. PubMed PMID: 27166375; PubMed Central PMCID: PMCPMC4987940.
26. Davis IW, Murray LW, Richardson JS, Richardson DC. MOLPROBITY: structure validation and all-atom contact analysis for nucleic acids and their complexes. Nucleic Acids Res. 2004;32(Web

644 Server issue):W615-9. Epub 2004/06/25. doi: 10.1093/nar/gkh398. PubMed PMID: 15215462;
645 PubMed Central PMCID: PMCPMC441536.
646 27. Schrödinger L DW. PyMOL. Internet access 2024.
647 28. Knudsen AS, Walker MR, Agullet JP, Bjornsson KH, Bassi MR, Barfod L. Enhancing
648 neutralization of Plasmodium falciparum using a novel monoclonal antibody against the rhoptry-
649 associated membrane antigen. Sci Rep. 2022;12(1):3040. Epub 2022/02/25. doi: 10.1038/s41598-
650 022-06921-1. PubMed PMID: 35197516; PubMed Central PMCID: PMCPMC8866459.
651 29. Soltermann F, Foley EDB, Pagnoni V, Galpin M, Benesch JLP, Kukura P, et al. Quantifying
652 Protein-Protein Interactions by Molecular Counting with Mass Photometry. Angew Chem Int Ed
653 Engl. 2020;59(27):10774-9. Epub 2020/03/14. doi: 10.1002/anie.202001578. PubMed PMID:
654 32167227; PubMed Central PMCID: PMCPMC7318626.
655 30. Pronk S, Pall S, Schulz R, Larsson P, Bjelkmar P, Apostolov R, et al. GROMACS 4.5: a high-
656 throughput and highly parallel open source molecular simulation toolkit. Bioinformatics.
657 2013;29(7):845-54. Epub 2013/02/15. doi: 10.1093/bioinformatics/btt055. PubMed PMID:
658 23407358; PubMed Central PMCID: PMCPMC3605599.
659 31. Dari Kimanius KJ, Max E Wilkinson, Sofia Lövestam, Vaithish Velazhahan, Takanori Nakane,
660 Sjors H.W. Scheres. Data-driven regularisation lowers the size barrier of cryo-EM structure
661 determination. bioRXiv. 2023.
662 32. Rohou A, Grigorieff N. CTFFIND4: Fast and accurate defocus estimation from electron
663 micrographs. J Struct Biol. 2015;192(2):216-21. Epub 2015/08/19. doi: 10.1016/j.jsb.2015.08.008.
664 PubMed PMID: 26278980; PubMed Central PMCID: PMCPMC6760662.
665 33. Bepler T, Morin A, Rapp M, Brasch J, Shapiro L, Noble AJ, et al. Positive-unlabeled
666 convolutional neural networks for particle picking in cryo-electron micrographs. Nat Methods.
667 2019;16(11):1153-60. Epub 2019/10/09. doi: 10.1038/s41592-019-0575-8. PubMed PMID:
668 31591578; PubMed Central PMCID: PMCPMC6858545.
669 34. Pang Y, Gordon R. Optical trapping of a single protein. Nano Lett. 2012;12(1):402-6. Epub
670 20111216. doi: 10.1021/nl203719v. PubMed PMID: 22171921.
671 35. Yousefi A, Ying C, Parmenter CDJ, Assadipapari M, Sanderson G, Zheng Z, et al. Optical
672 Monitoring of In Situ Iron Loading into Single, Native Ferritin Proteins. Nano Lett. 2023;23(8):3251-
673 8. Epub 20230413. doi: 10.1021/acs.nanolett.3c00042. PubMed PMID: 37053043; PubMed Central
674 PMCID: PMCPMC10141409.
675 36. Xu H, Jones S, Choi BC, Gordon R. Characterization of Individual Magnetic Nanoparticles in
676 Solution by Double Nanohole Optical Tweezers. Nano Lett. 2016;16(4):2639-43. Epub 20160318.
677 doi: 10.1021/acs.nanolett.6b00288. PubMed PMID: 26977716.
678 37. Shan L, Mathews, II, Khosla C. Structural and mechanistic analysis of two prolyl
679 endopeptidases: role of interdomain dynamics in catalysis and specificity. Proc Natl Acad Sci U S A.
680 2005;102(10):3599-604. Epub 2005/03/02. doi: 10.1073/pnas.0408286102. PubMed PMID:
681 15738423; PubMed Central PMCID: PMCPMC553306.
682 38. Hajizadeh NR, Franke D, Jeffries CM, Svergun DI. Consensus Bayesian assessment of protein
683 molecular mass from solution X-ray scattering data. Sci Rep. 2018;8(1):7204. Epub 2018/05/10. doi:
684 10.1038/s41598-018-25355-2. PubMed PMID: 29739979; PubMed Central PMCID:
685 PMCPMC5940760.
686 39. Mohammad T, Amir M, Prasad K, Batra S, Kumar V, Hussain A, et al. Impact of amino acid
687 substitution in the kinase domain of Bruton tyrosine kinase and its association with X-linked
688 agammaglobulinemia. Int J Biol Macromol. 2020;164:2399-408. Epub 2020/08/14. doi:
689 10.1016/j.ijbiomac.2020.08.057. PubMed PMID: 32784026.

690 40. Liebschner D, Afonine PV, Baker ML, Bunkoczi G, Chen VB, Croll TI, et al. Macromolecular
691 structure determination using X-rays, neutrons and electrons: recent developments in Phenix. Acta
692 Crystallogr D Struct Biol. 2019;75(Pt 10):861-77. Epub 2019/10/08. doi:
693 10.1107/S2059798319011471. PubMed PMID: 31588918; PubMed Central PMCID:
694 PMCPMC6778852.
695 41. Correia BE, Bates JT, Loomis RJ, Baneyx G, Carrico C, Jardine JG, et al. Proof of principle for
696 epitope-focused vaccine design. Nature. 2014;507(7491):201-6. Epub 2014/02/07. doi:
697 10.1038/nature12966. PubMed PMID: 24499818; PubMed Central PMCID: PMCPMC4260937.
698 42. Walter TS, Meier C, Assenberg R, Au KF, Ren J, Verma A, et al. Lysine methylation as a routine
699 rescue strategy for protein crystallization. Structure. 2006;14(11):1617-22. Epub 2006/11/14. doi:
700 10.1016/j.str.2006.09.005. PubMed PMID: 17098187; PubMed Central PMCID: PMCPMC7126202.
701 43. Herzik MA, Jr., Wu M, Lander GC. High-resolution structure determination of sub-100 kDa
702 complexes using conventional cryo-EM. Nat Commun. 2019;10(1):1032. Epub 2019/03/06. doi:
703 10.1038/s41467-019-08991-8. PubMed PMID: 30833564; PubMed Central PMCID:
704 PMCPMC6399227.
705 44. Lyumkis D. Challenges and opportunities in cryo-EM single-particle analysis. J Biol Chem.
706 2019;294(13):5181-97. Epub 2019/02/26. doi: 10.1074/jbc.REV118.005602. PubMed PMID:
707 30804214; PubMed Central PMCID: PMCPMC6442032.
708 45. Awasthi S, Ying C, Li J, Mayer M. Simultaneous Determination of the Size and Shape of Single
709 alpha-Synuclein Oligomers in Solution. ACS Nano. 2023;17(13):12325-35. Epub 2023/06/16. doi:
710 10.1021/acsnano.3c01393. PubMed PMID: 37327131; PubMed Central PMCID: PMCPMC10339783.

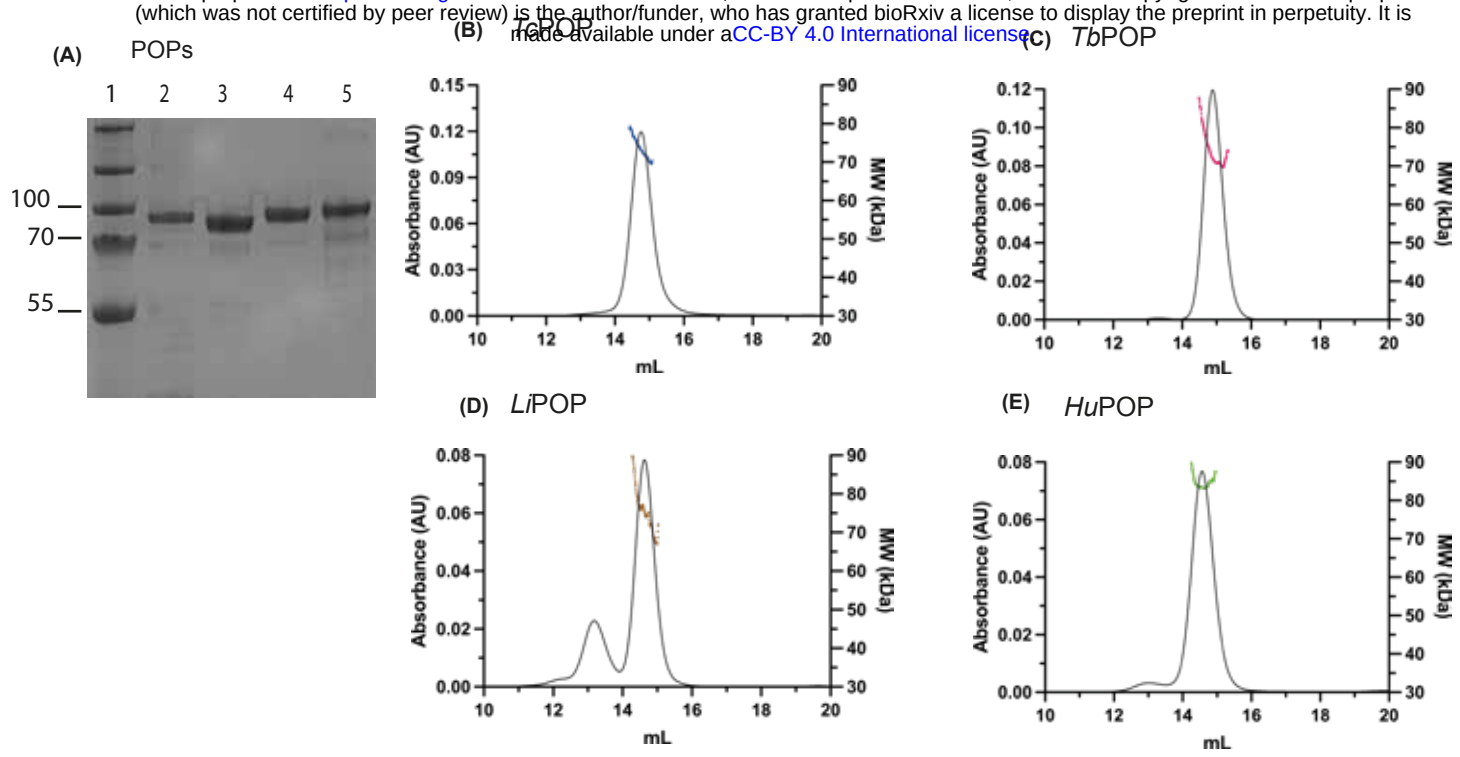

Figure 1. Expression and purification of recombinant prolyl oligopeptidases (POPs) from *E. coli*.
(A) SDS-PAGE of POPs samples from affinity chromatography experiments: 1= Protein MW ladder (kDa), 2= *Trypanosoma cruzi* POP (*Tc*POP), 3= *Trypanosoma brucei* POP (*Tb*POP), 4= *Leishmania major* POP (*Li*POP) and *Homo sapiens* POP (*Hu*POP). SEC-MALS experiments, using a S200 10/300 confirmed the theoretical molecular mass values for each POP (B-E) of ~ 78 kDa, corresponding to ~ 13 mL elution volume.

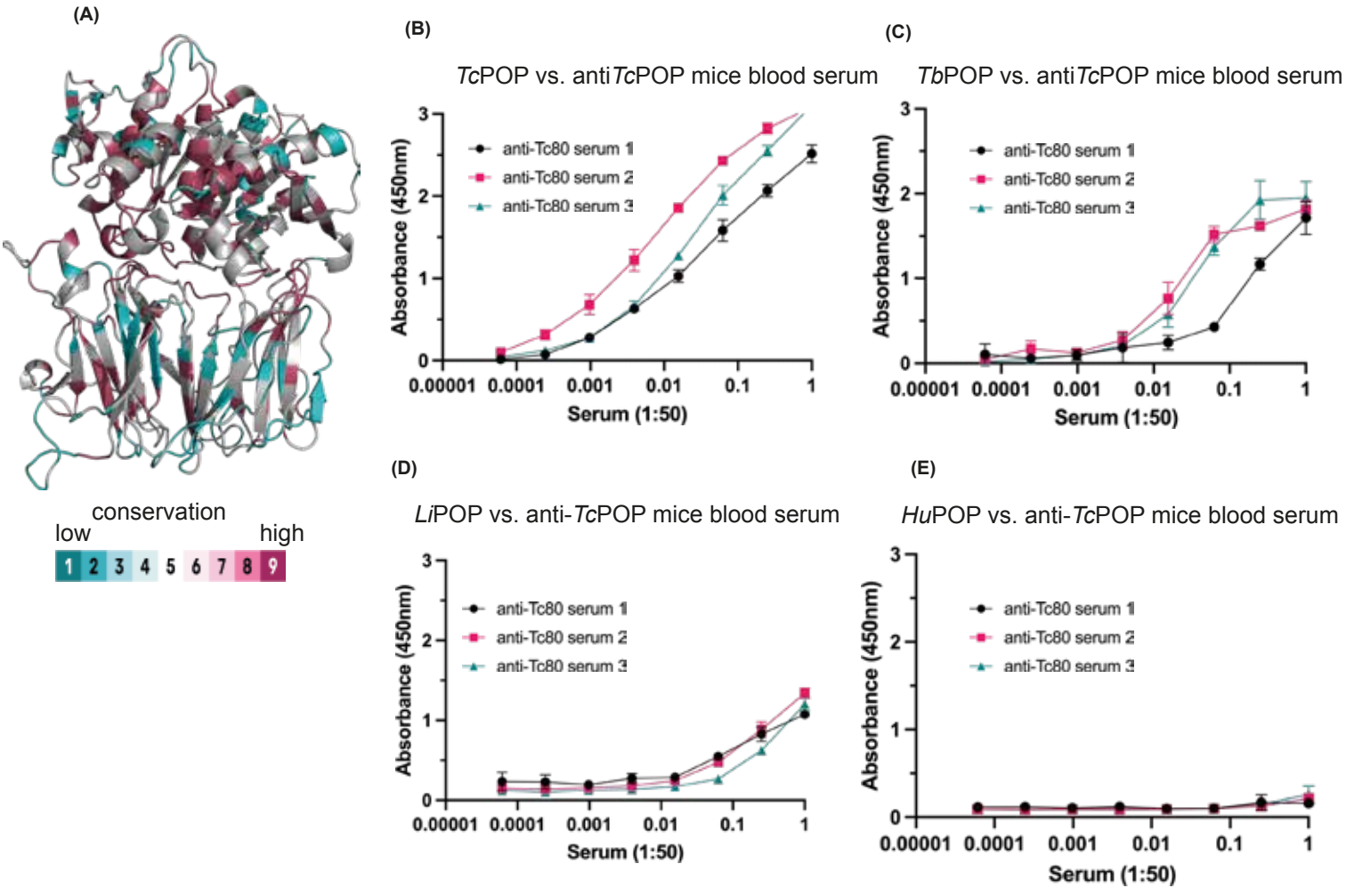

Figure 2. ELISA testing of anti-*Tc*80 polyclonal serum against recombinant POPs. (A) Sequence conservation was mapped with CONSURF on the AlphaFold model of *Tc*POP highlighting the conservation across the family in the two domains (ranging between cyan and purple i.e. low to high conservation, respectively). (B) *Tc*POP was used to immunise mice and polyclonal serum (diluted 1:50) v/v and tested agains recombinant *Tc*POP, (C) *Tb*POP, (D) *Li*POP and (E) *Hu*POP to assess cross-reactivity across species. Negative controls using buffer alone or BSA did not produce any signal.

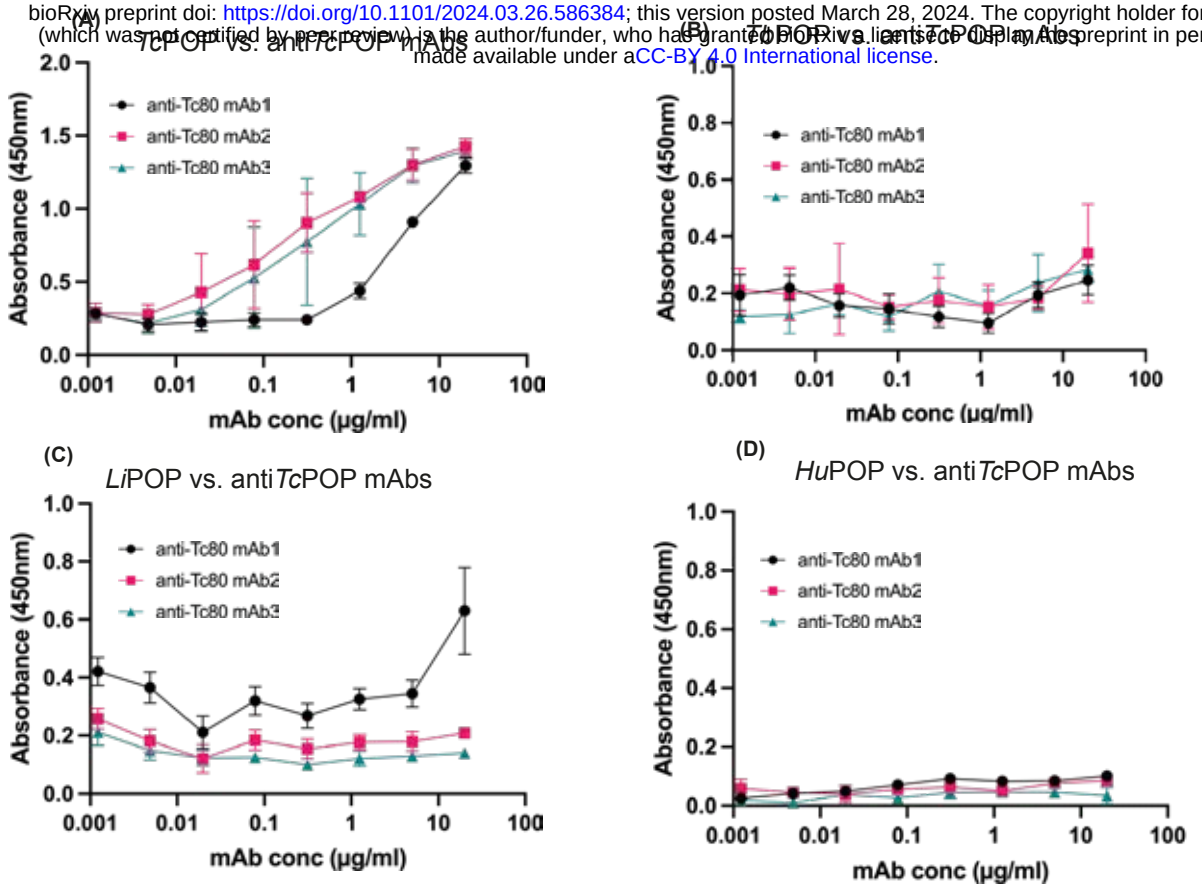

Figure 3. ELISA testing of anti-*Tc*POP monoclonal antibodies against recombinant *Tc*POP and its homologues. Three monoclonal IgG1 antibodies (mAbs 1-3) were isolated and purified from hybridomas and tested by ELISA against plates coated with: recombinant *Tc*POP, originally used for immunisation (A), *Trypanosoma brucei* POP (*Tb*POP) (B), *Leishmania infantum* POP (*Li*POP) (C) or *Homo sapiens* POP (*Hu*POP).

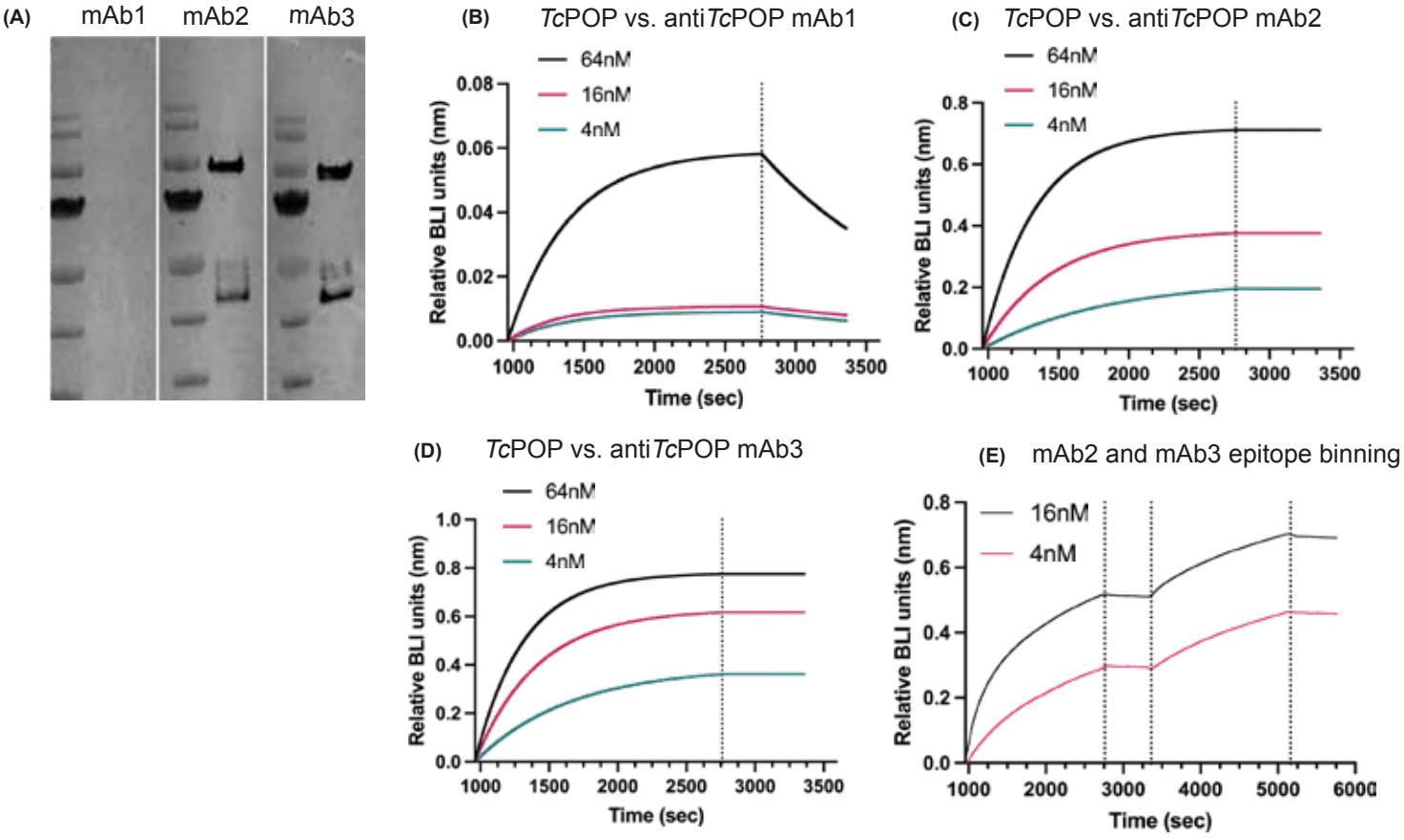

Figure 4. Testing of anti-*Tc*POP monoclonal antibodies by Western blot and Biolayer Interferometry. (A) The three monoclonal antibodies (mAbs 1-3) were conjugated to HRP and tested by Western blot for the identification of denatured antingen. Whilst mAb2 and mAb3 recognised the denatured antigen, mAb1 did not, indicating that in mAb1 the epitope could be conformational. (B-D) Sensograms of BLI experiments using the same range of TcPOP antigen concentrations (4-16 nM) were recorded using Octet 4 (Sartorius). The experiments were performed for 3500 seconds at 25°C in triplicates. (B) mAb1 showed slower kon and fastest koff, whilst mAb2 and mAb3 showed similar kon but very slow koff. (E) Additionally, epitope binning experiments with mAb3 on top of mAb2, suggest that they do not share the same identical epitopes.

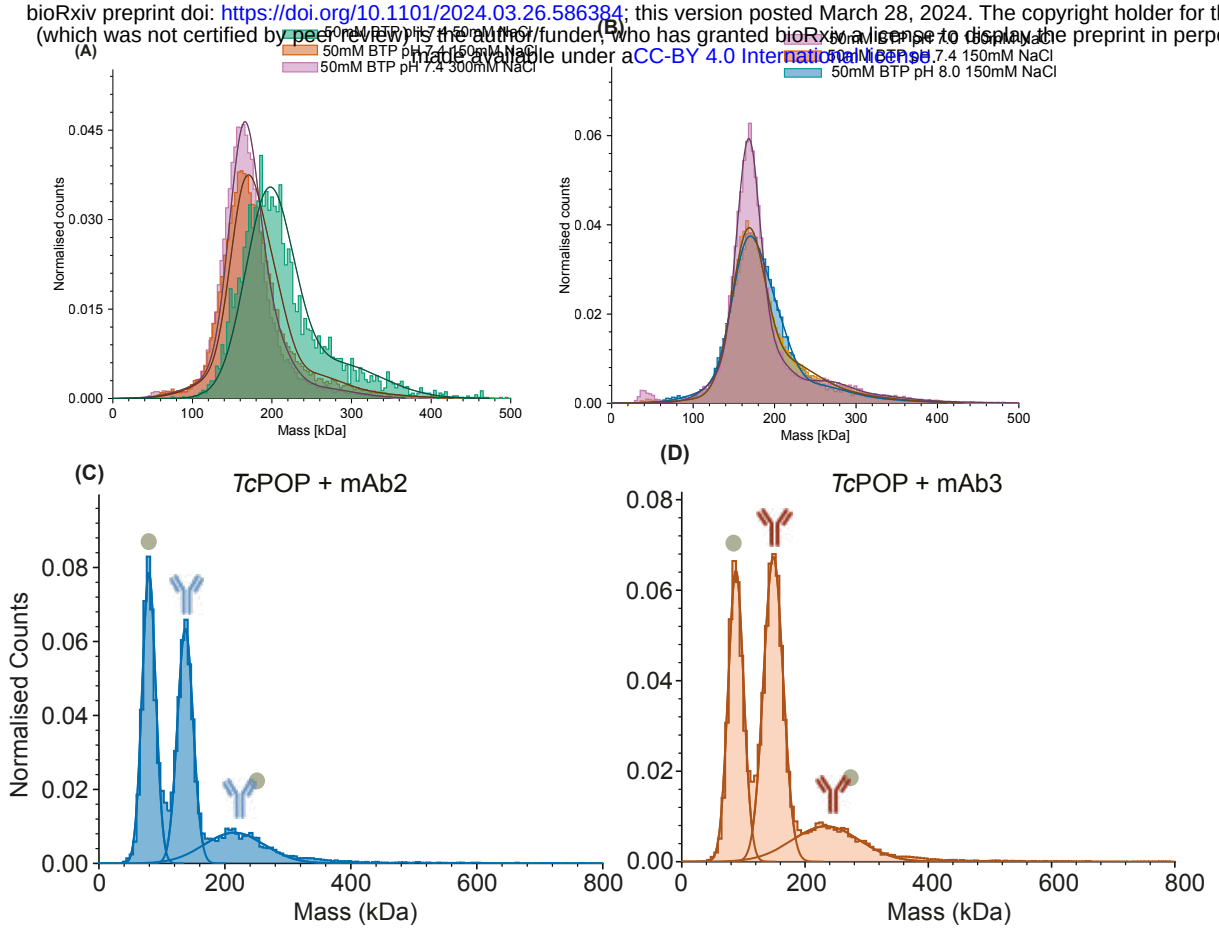

Figure 5. Mass photometry measurement of *Tc*POP and mAbs. Buffer conditions for symmtertic distribution of particles were measured across (A) different NaCl concentrations, (B) followed by different pH, determining the condition for optimal *Tc*POP stability.Furthermore, the binidng of mAb2 (C) and mAb3 (D) with *Tc*POP was analysed as shown.

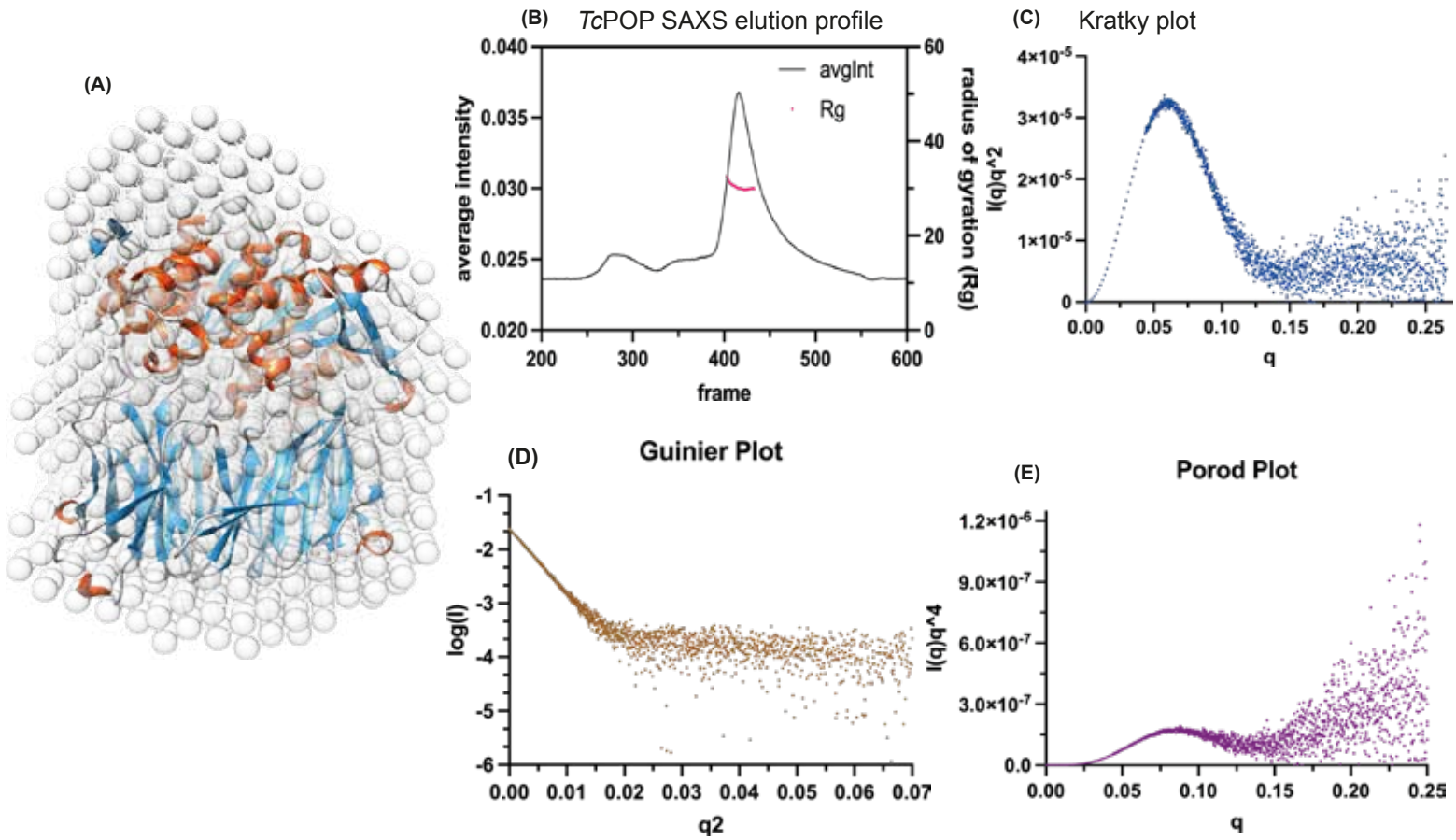

Figure 6. SEC-SAXS analysis of *Tc*POP. (A) SEC-SAXS based ab initio determination of low-resolution density of *Tc*POP built using DAMMIN, implemented in ATSAS package, showed fitting with Alphafold model of *Tc*POP. (B) SEC-SAXS elution profile across radius of gyration (Rg) showed *Tc*POP overall mass distribution and compactness, (C) Kratky plot, (D) Guinier plot and (E) Porod confirmed plausibly globular and compact shape of *Tc*POP in solution.

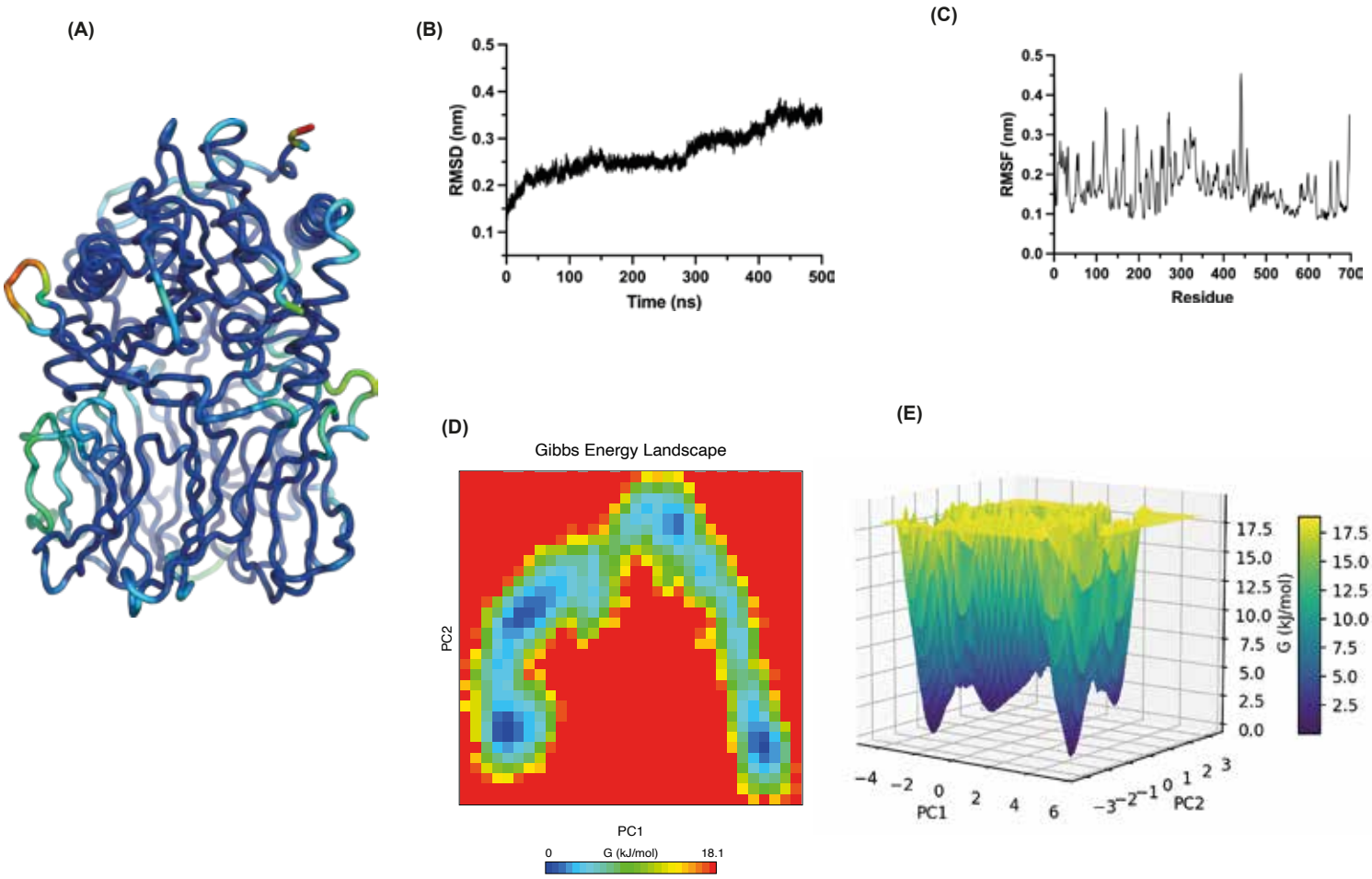

Figure 7. Time evolution and structural dynamics of *Tc*POP over 500ns. (A) Estimating range of B-factor values, blue (more stable) and Red (highly unstable) (B) RMSD against the C-alpha backbone and (C) residual fluctuations during the course of simulation. Gibbs free energy landscape generated during the simulation of *Tc*POP, (D) 2D projection and (E) 3D basins were plotted against the principal component axis

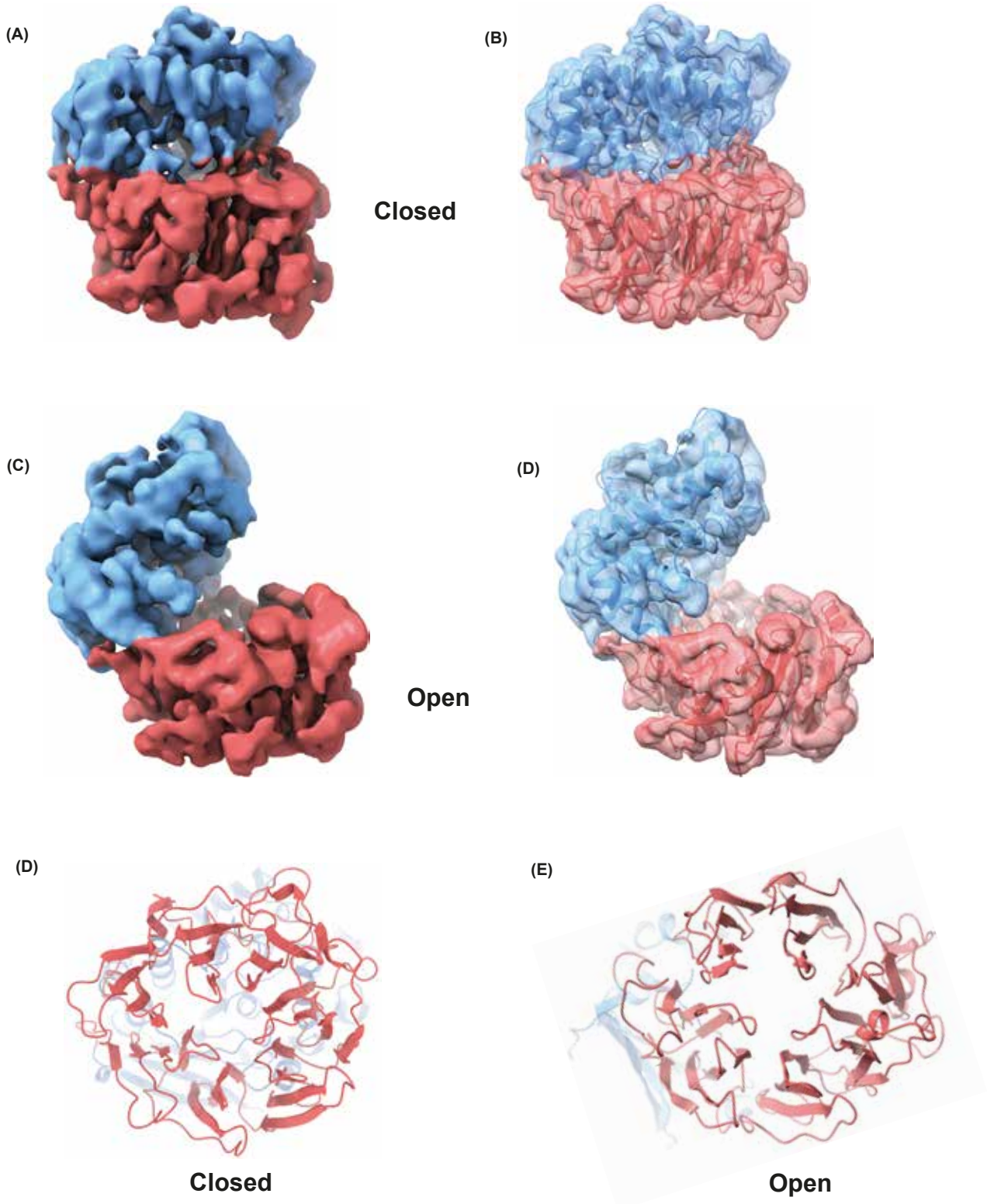

Figure 8. Cryo-EM structure determination of *Tc*POP. (A) Cryo-EM map of closed conformation of *Tc*POP resolved at 2.5Å resolution, (B) docked with refined AlphaFold model and (C) open conformation of *Tc*POP resolved at 3Å resolution, (D) docked with refined homology model of *Tc*POP. (E,F) representation of the presence of β-propeller pore in the closed and open conformation of *Tc*POP, confirming the presence of pore in both the conformational states. Video shows the transition between both the domains in the supplementary data.